Three-dimensional CFD study of conical spouted beds containing heavy particles: Design parameters

Naimeh Setarehshenas*, Seyyed Hossein Hosseini**,†, Mohsen Nasr Esfahany***, and Goodarz Ahmadi****

*Department of Chemical Engineering, University of Sistan and Baluchestan, Zahedan 98164-161, Iran
**Department of Chemical Engineering, Ilam University, Ilam 69315-516, Iran
***Department of Chemical Engineering, Isfahan University of Technology, Isfahan 84156-83111, Iran
****Department of Mechanical and Aeronautical Engineering, Clarkson University, Potsdam, NY 13699-5725, U.S.A.

Abstract–The flow behavior of conical spouted beds containing heavy particles that occurs in chemical vapor deposition (CVD) was investigated using the computational fluid dynamics (CFD) approach. A fully Eulerian description of solid and gas phases flows in 3D was used in these simulations. The hydrodynamics parameters including particle velocity, solid flux, and solid volume fraction profiles at different bed levels were evaluated, and the overall behavior of solid particles in the beds was studied. The results showed close agreement with the corresponding experimental data. The effects of cone angle, static bed height, and cone bottom diameter on the hydrodynamic behavior of heavy particles were analyzed and the results were presented. In addition, the effects of flat wall of semi-conical spouted bed (half-column) on the CFD results and performance of the spouted bed were investigated. The hydrodynamic results for the full bed were quite different from those for the half bed geometries. It was also found that the conical spouted bed with the angle of 45° leads to the roughly stable spouting compared to the 30° angle bed. The CFD model also showed that the conical-cylindrical spouted beds operating with heavy particles has the potential for periodic occurrence of choking in the spout zone.

Keywords: CFD, Conical Spouted Bed, Heavy Particles, Hydrodynamics, Design Parameters

INTRODUCTION

The original spouted bed was first developed by Gishler [1] for drying moist wheat particles as a replacement for the slugging fluidized bed. Typically, a spouted bed has three distinct regions: spout, annulus, and fountain. Today, the spouted bed is extensively used in various industrial applications such as drying of grains, spray drying, coating, heterogeneous catalysis, combustion, and gasification of biomass and coal [2-9]. For the spouted beds systems, it is imperative to note the distinction between conical and conical-cylindrical spouted beds, before presenting the literature review of the subject. In the former, the solid particles mainly fills the conical section, while, in the latter, a large portion of solid particles is processed in the cylindrical region.

Although new techniques in the experimental studies of spouted beds have provided useful information [10-15], computer simulation methodologies have also evolved into valuable tools for acquiring detailed information regarding gas and solid particles behaviors in spouted beds [16-20]. With the continuing advances in computing capabilities and the development of robust numerical algorithms, computational fluid dynamics (CFD) has emerged as an important tool for studying the complex flow behavior of gas-solid multiphase systems.

Several CFD studies of various types of spouted beds such as conical-cylindrical spouted beds [18], conical-cylindrical spouted beds with draft tube [19,20] and pseudo 2D spouted beds [22-24] have been reported in the literature. While all these studies are concerned with light particles, there is a limited number of studies conducted in spouted beds of heavy particles with $\rho > 3,000 \, kg/m^3$. Some previous researchers found that the particle density greatly affects the hydrodynamic behavior in the bed [25,26]. Recently, Zhou and Bruns [27] reported that various relations that were derived for the low density particles (light particles) in spouted beds predict results that deviate significantly from the experimental data for heavy ZrO_2 particles. They also developed a new expression for the minimum spouting velocity for shallow conical spouted beds operating with heavy particles.

A few studies have been reported in the literature for the hydrodynamics of conical spouted beds containing heavy particles with densities of about $6,000 \, kg/m^3$. Using the CFD code MFIX and an axisymmetric model, Pannala et al. [28] investigated a conical spouted bed containing heavy zirconia particles, and reported incoherent spouting in the bed. Lüle et al. [29] performed a 2D CFD simulation of a conical spouted bed containing zirconia particles and investigated some geometrical design parameters. More recently, Setarehshenas et al. [30] studied a 3D conical spouted bed with heavy particles, Zirconia, using the commercial CFD code, ANSYS-Fluent (version 15). They evaluated the effect of the solid wall boundary conditions, as well as, the use of different drag functions. The above brief literature survey suggests that further detailed investi-

gations are required to provide a better understanding of the spouted bed operating condition with heavy particles.

One important application of conical spouted beds, including heavy particles, is the coating of uranium dioxide kernels with carbon and silicon carbide layers to produce nuclear fuel of spherical tristructural-isotropic (TRISO) by chemical vapor deposition (CVD), which is performed at high temperatures [28,29]. Therefore, detailed hydrodynamics of conical spouted bed reactors is necessary for design, scale-up, and developing a fabrication process of these fuel coaters. We chose zirconia particles because their properties are the same as TRISO particles, especially their density is comparable.

In light of the above brief review, in the present study the flow behavior of the 3D conical spouted beds operating with heavy particles with a density of 6,050 kg/m^3 was investigated using the computational fluid dynamics (CFD) approach. In this study, some hydrodynamics parameters, namely, particle velocity, solid flux, and solid volume fraction profiles at different bed levels, were evaluated by CFD, and the overall behavior of solid particles in the bed was studied. Impact of some design parameters such as cone angle, static bed height, and cone bottom diameter of the bed on the hydrodynamics of heavy particles at the same operating conditions were studied. In addition, the influence of flat wall of semi-conical spouted bed (half-column) on the particles behavior was also studied. The new findings regarding the effect of design parameters of the conical spouted beds containing heavy particles were also discussed.

METHODS

1. CFD Model for the Conical Spouted Beds with Heavy Particles

An Eulerian-Eulerian gas-solid model was used for simulating the complex flow behavior in a three-dimensional conical spouted bed including heavy zirconia particles. In this method continuous gas phase and the dispersed particles phase are treated as interpenetrating continua. The solid-phase is assumed to be spherical particles with uniform diameter.

The governing equations are listed in Table 1. Since the solid phase is treated as a fluid in the Eulerian-Eulerian gas-solid model, it is required to close the governing equations constitutive relations

for the solid phase viscosity and pressure. The constitutive models used in the present simulations are listed in Table 2. The fluctuation of particles and the inter-particle collisions are accounted for as a function of the granular temperature using the kinetic theory of granular flows (KTGF). In this study, the full granular temperature equation given by Eq. (T1-6) is used in the simulations. The granular temperature is needed in the constitutive equations for pressure and viscous stress of the particulate phase. The virtual mass and the lift force, as well as, particle rotational effects are neglected. For the solid phase, the solid shear viscosity is composed of collisional, kinetic and frictional effects. For very dense flows, the friction created between the particles generates a large amount of stress. The expression of Schaeffer [31] is used to model the frictional viscosity in the dense region. The bulk viscosity and the solid pressure are evaluated using the expressions suggested by Lun et al. [32]. The gas-solid interphase exchange coefficient, β, is modeled using the expression of Gidaspow et al. [33] that includes a switching function.

2. Simulation Method

2-1. Simulation Conditions

For code verification, the predicted CFD results were compared with the experimental data of the conical spouted bed operated by Kulah et al. [10] and Lüle et al. [29]. Their measurements were performed in a conical spouted bed with different cone angle filled with 1.0 mm spherical zirconia particles with density of 6,050 kg/m^3. The bed was made of polyoxymethylene, Fig. 1(a) shows a schematic diagram of the spouted bed used by Kulah et al. [10] and Lüle et al. [29], and the relevant geometric parameters are summarized in Table 3. In the present study, all simulations were performed for the exact condition of the experiment of [10,29]. The corresponding values of parameters used in the current simulations are in Table 4. In the experiment, air at ambient condition was used as the spouting gas and was introduced from the central nozzle shown in Fig. 1. Kulah et al. [10] and Lüle et al. [29] used a fiber optic probe technique to measure instantaneous axial particle velocity and solid volume fraction at several axial levels. Fig. 1(d) shows the schematic of half column for the cone angle of 30° that is also studied in the present work to examine the influence of bed geometry on the particle velocity. In this figure the planes that are used for

Table 1. Governing equations used in the present simulations

1. *Continuity equations of gas and solid phases*

$$\frac{\partial}{\partial t}(\alpha_g \rho_g) + \nabla \cdot (\alpha_g \rho_g \vec{\upsilon}_g) = 0 \tag{T1-1}$$

$$\frac{\partial}{\partial t}(\alpha_s \rho_s) + \nabla \cdot (\alpha_s \rho_s \vec{\upsilon}_s) = 0 \tag{T1-2}$$

$$\alpha_s + \alpha_g = 1 \tag{T1-3}$$

2. *Momentum equations of gas and solid phases*

$$\frac{\partial}{\partial t}(\alpha_g \rho_g \vec{\upsilon}_g) + \nabla \cdot (\alpha_g \rho_g \vec{\upsilon}_g \vec{\upsilon}_g) = -\alpha_g \nabla P + \nabla \overline{\overline{\tau}}_g + \beta(\vec{\upsilon}_s - \vec{\upsilon}_g) + \alpha_g \rho_g g \tag{T1-4}$$

$$\frac{\partial}{\partial t}(\alpha_s \rho_s \vec{\upsilon}_s) + \nabla \cdot (\alpha_s \rho_s \vec{\upsilon}_s \vec{\upsilon}_s) = -\alpha_s \nabla P - \nabla P_s + \nabla \cdot \overline{\overline{\tau}}_s + \beta(\vec{\upsilon}_g - \vec{\upsilon}_s) + \alpha_s \rho_s g \tag{T1-5}$$

3. *Granular temperature equation (Ding and Gidaspow, 1990)*

$$\frac{3}{2}\left[\frac{\partial}{\partial t}(\rho_s \alpha_s \Theta_s) + \nabla \cdot (\alpha_s \rho_s \vec{\upsilon}_s \Theta_s)\right] = (-\nabla P_s \overline{I} + \overline{\overline{\tau}}_g): \nabla \vec{\upsilon}_s + \nabla \cdot (k_s \nabla \Theta_s) - \gamma_s - 3\beta \Theta_s \tag{T1-6}$$

Table 2. Constitutive equations used in the present simulations

1. *Solid and gas phase stress tensors*

$$\bar{\bar{\tau}}_g = \alpha_g \mu_g \left\{ [\nabla \vec{\upsilon}_g + (\nabla \vec{\upsilon}_g)^T] - \frac{2}{3} \nabla \cdot \vec{\upsilon}_g \bar{I} \right\} \tag{T2-1}$$

$$\bar{\bar{\tau}}_s = \alpha_s \mu_s [\nabla \vec{\upsilon}_s + (\nabla \vec{\upsilon}_s)^T] + \left(\alpha_s \lambda_s - \frac{2}{3} \alpha_s \mu_s \right) \nabla \cdot \vec{\upsilon}_s \bar{I} \tag{T2-2}$$

2. *Solid pressure*

$$P_s = \alpha_s \rho_s \Theta_s + 2\rho_s(1+e_s)\alpha_s^2 g_0 \Theta_S \tag{T2-3}$$

4. *Solid shear viscosity*

$$\mu_s = \mu_{s,\,col} + \mu_{s,\,kin} + \mu_{s,\,fr} \tag{T2-4}$$

5. *Collisional viscosity*

$$\mu_{s,\,col} = \frac{4}{5} \alpha_s \rho_s d_s g_0 (1+e_s) \left(\frac{\Theta_s}{\pi} \right)^{1/2} \tag{T2-5}$$

6. *Kinetic viscosity*

$$\mu_s = \frac{\alpha_s d_s \rho_s \sqrt{\Theta_s \pi}}{6(3-e_s)} \left[1 + \frac{2}{5}(1+e_s)(3e_s-1)\alpha_s g_0 \right] \tag{T2-6}$$

7. *Frictional viscosity*

$$\mu_{s,\,fr} = \frac{P_s \sin\phi}{2\sqrt{I_{2D}}} \tag{T2-7}$$

8. *Solid bulk viscosity*

$$\lambda = \frac{4}{3} \alpha_s \rho_s d_s g_0 (1+e_s) \sqrt{\frac{\Theta_s}{\pi}} \tag{T2-8}$$

9. *Diffusion coefficient of granular energy*

$$k_{\Theta_s} = \frac{150 \rho_s d_s \sqrt{\pi \Theta_s}}{384(1+e_s)g_0} \left[1 + \frac{6}{5}\alpha_s g_0(1+e_s) \right]^2 + 2\alpha_s \rho_s d_s g_0(1+e_s) \left(\frac{\Theta_s}{\pi} \right)^{1/2} \tag{T2-9}$$

10. *Collisional energy dissipation*

$$\gamma_s = \frac{12(1-e_s^2)g_0}{d_s \sqrt{\pi}} \rho_s \alpha_s^2 \Theta_s^{3/2} \tag{T2-10}$$

11. *Radial distribution function*

$$g_0 = \left[1 - \left(\frac{\alpha_s}{\alpha_{s,\,max}} \right)^{1/3} \right]^{-1} \tag{T2-11}$$

12. *Gas-solid drag coefficient*

$$\beta = (1-\varphi_{gs})\beta_{Ergun} + \varphi_{gs}\beta_{Wen-Yu} \quad \text{where}$$

$$\beta_{Ergun} = 150 \frac{\alpha_s^2 \mu_g}{\alpha_s d_s^2} + 1.75 \frac{\alpha_s \rho_g |\vec{\upsilon}_s - \vec{\upsilon}_g|}{d_s} \quad \text{for } \alpha_g \leq 0.8$$

$$\beta_{Wen-Yu} = \frac{3}{4} C_D \frac{\alpha_s \alpha_g \rho_g |\vec{\upsilon}_s - \vec{\upsilon}_g|}{d_s} \alpha_g^{-2.65} \quad \text{for } \alpha_g > 0.8$$

$$C_D = \begin{cases} \frac{24}{\alpha_g Re_s}[1 + 0.15(\alpha_g Re_s)^{0.687}], & Re_s < 1000 \\ C_D = 0.44, & Re_s \geq 1000 \end{cases} \quad \text{in which, } Re_s = \frac{\rho_g |\vec{\upsilon}_s - \vec{\upsilon}_g| d_s}{\mu_g}$$

$$\varphi_{gs} = \frac{\text{Arctan}[150 \times 1.75(0.2 - \alpha_s)]}{\pi} + 0.5 \tag{T2-12}$$

showing the contour plots of solid volume fraction are also specified.

2-2. Initial and Boundary Conditions

For the initial conditions, the solid volume fraction in the spouted bed was set at 0.6, and the gas velocity inside the spouted bed was set to zero. The solid volume fraction in the freeboard region was also set to zero. A boundary condition at the bottom of the bed was used to specify a uniform gas inlet velocity. A no-slip bound-ary condition for all walls was assumed for the gas phase. Johnson and Jackson [34] wall boundary condition was applied for the tangential velocity, and granular temperature of the solid phase at the walls.

2-3. Solution Procedure

The CFD code ANSYS-FLUENT (version 15) was used to simulate the hydrodynamics of the 3D conical spouted beds that were
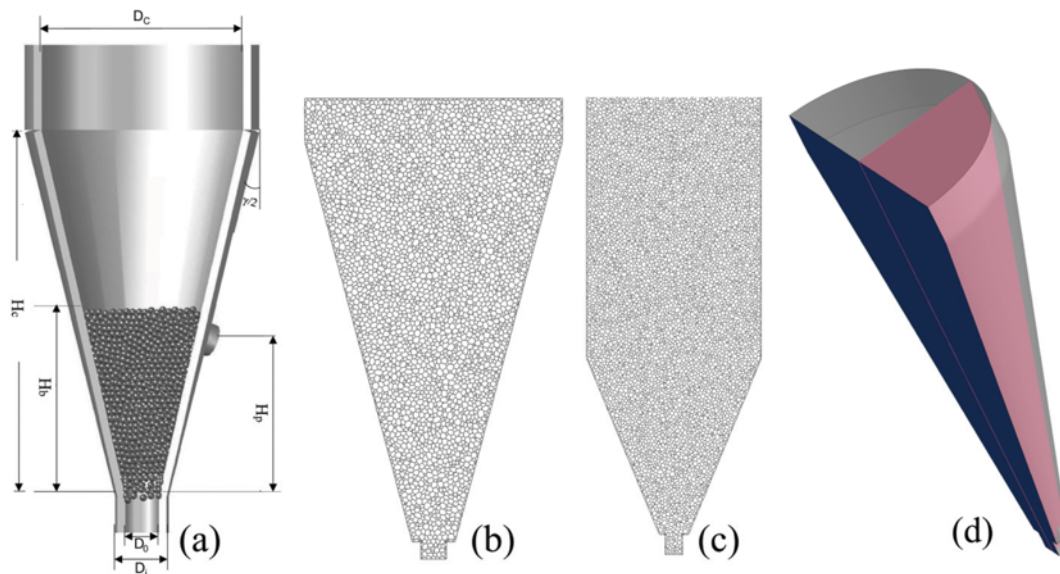
Fig. 1. Schematic diagram of (a) geometry, (b) grids of the spouted bed with 30° cone angle, and (c) grids of the spouted bed with 45° cone angle, (d) Structure of half column with cone angle of 30°.

Table 3. Geometric parameters of the spouted beds of experiments of Kulah et al. [10] and Lüle et al. [29] as well as simulations

γ (deg)	D_o (mm)	D_i (mm)	D_c (mm)	H_c (mm)	H_b (mm)	U_{ms} (m/s)	U (m/s)
30	15	25	150	233	140	30.9	38.6
45	15	25	150	151	100	29.5	36.9
					140	45.6	57.0

Table 4. Parameters used for simulation of experiments of Kulah et al. [10] and Lüle et al. [29]

Description	Symbol	Value
Gas density	ρ_g (kg/m^3)	1.22
Gas viscosity	μ_g (kg/m s)	1.789×10^{-5}
Gas velocity	V (m/s)	$1.25 U_{ms}$
Particle-particle restitution coefficient	e_s (-)	0.9
Particle-wall restitution coefficient	e_w (-)	0.99
Specularity coefficient	φ (-)	0.05
Loose packing volume fraction	α_s (-)	0.6
Maximum volume fraction of particles	$\alpha_{s,\,max}$ (-)	0.61

used in the experiments of Kulah et al. [10] and Lüle et al. [29]. The set of governing equations described in Table 1 was solved by a finite volume technique. The phase coupled SIMPLE algorithm, which is an extension of the SIMPLE algorithm for multiphase flow, was used for the pressure-velocity coupling and correction. A first-order upwind scheme was utilized for the volume fraction term, while a second-order upwind discretization scheme was used for momentum and granular temperature equations, which are consistent with the earlier works [35-37]. A transient simulation was performed, using a time step of 5×10^{-5} s with 35 iterations per time step. A convergence criterion of 10^{-3} for each scaled residual component was used for the relative error between two successive iterations. Fig. 1(b), (c) shows the computational grids for the conical

spouted beds with different cone angles. As seen from the figure, the polyhedral grid structure for the computational domain was used. The polyhedral mesh was derived directly from the tetrahedral mesh by forming polygons around each node in the tetrahedral mesh in ANSYS-FLUENT 15.0. The grid independency was investigated and the results were reported in a previous work [30], and for sake of brevity are not repeated here. Supermicro Workstation 2x Intel Xeon E-5646 2.4 GHz (24 computing nodes) & 32 GB RAM was used for performing the simulations.

RESULTS AND DISCUSSION

Simulation results showed that after five seconds the quasi-steady state was reached; therefore, the time averages of flow variables were computed for the time duration of 5 s to 10 s. The CFD results of time-averaged particles velocity and solid volume fraction at the height of H_p=100 mm for the spouted bed with 30° cone angle, inlet velocity U=38.6 m/s ($1.25U_{ms}$) and initial bed height of H_b= 140 mm are plotted in Fig. 2 and compared with the experimental data of Lüle et al. [29]. Both experimental data and CFD results in Fig. 2 show that the particle velocity has its maximum value on the bed axis and the velocity reduces towards the annulus region. The solid volume faction, however, has its minimum value at the bed axis in the spout region, and increases toward the annulus region. Particle velocities are in a close agreement with the measured data, while the solid volume fraction shows slight deviation in the spout region. Nonetheless, the predicted solid volume frac-
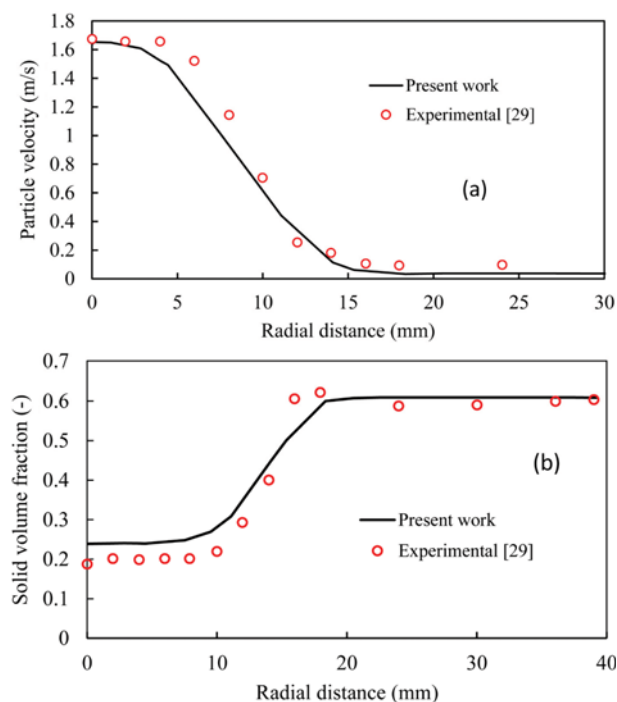
Fig. 2. Particle velocity (a) and solid volume fraction (b) for the spouted bed with 30° cone angle, U=38.6 m/s (1.25U_{ms}) and H_b=140 mm at H_p=100 mm.

tion profiles have the same trend of the experimental data of Lüle et al. [29].

For U=38.6 m/s (1.25U_{ms}) and H_b=140 mm, the instantaneous contour plots of solid volume fraction in the spouted bed with 30° cone angle are shown in Fig. 3. This figure shows distinct regions of spouted beds, namely, the spout where particles rise at high velocities, the annulus region between the spout and the column wall, where particles move downwards, and finally, the fountain in which particles rise in the core region to their highest positions and then rain back onto the periphery. Similar to the spouted beds operating with low density (light) particles, the concentration of particles is lower in the spout and fountain regions in comparison with the annulus region. Unlike the conical spouted beds of light particles, however, the spout continuously changes as the connected bubbles appear along that region for the conical spouted bed with heavy particles resulting in change of the flow pattern. Fig. 3 clearly indicates a pulsation process as the spout shape and the resulting fountain height are not steady and change periodically with time. Therefore, the unsteady behavior is manifested with the formation of a neck which starts at the gas inlet, propagates upward, and finally vanishes at the end of the spout within one cycle. When the particles move upward in the neck region, they interact with additional particles from the annulus zone, and the particle concentration increases and the suspension becomes denser at the end of the spout. This behavior is visible in the simulation results shown in Fig. 3. That is, the CFD model is capable of predicting the incoherent spouting, which is consistent with the experimental observation of conical spouted bed of heavy particles [28].

The CFD results of time-averaged particles velocity, solid volume fraction and solid flux at different bed levels for the spouted bed with cone angle of 45°, U=57 m/s (1.25U_{ms}) and H_b=140 mm
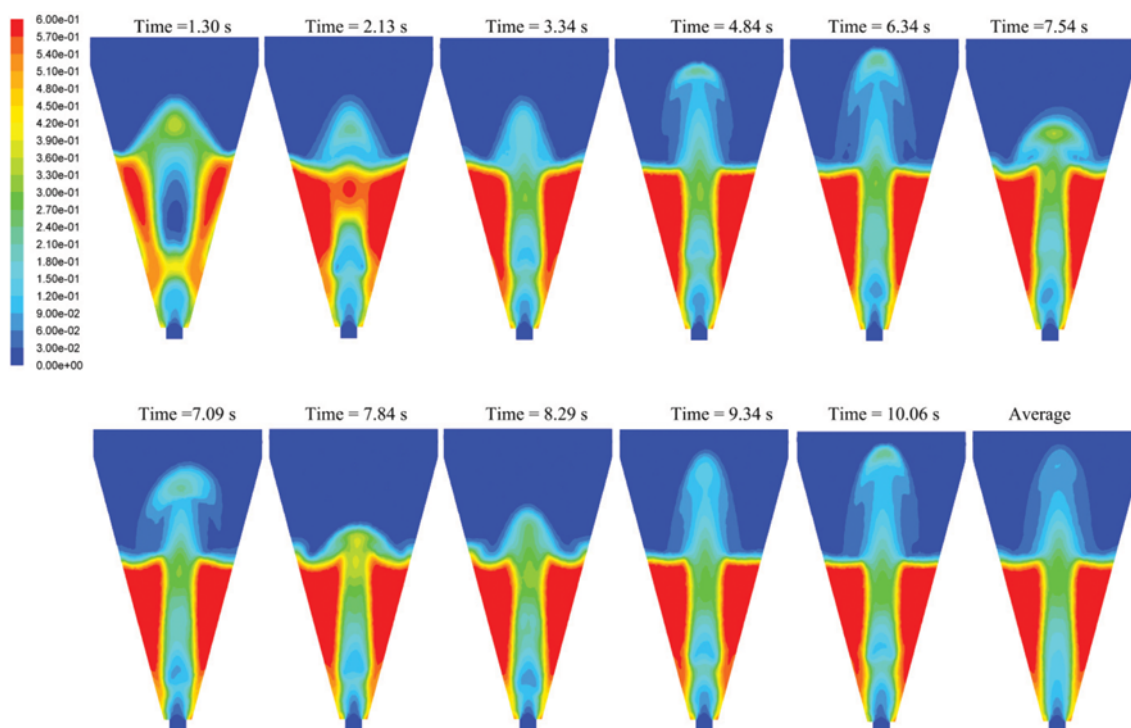

Fig. 3. Contour plots of solid volume fraction in the spouted bed with 30° cone angle, U=38.6 m/s and H_b=140 mm at different times and its time-averaged.
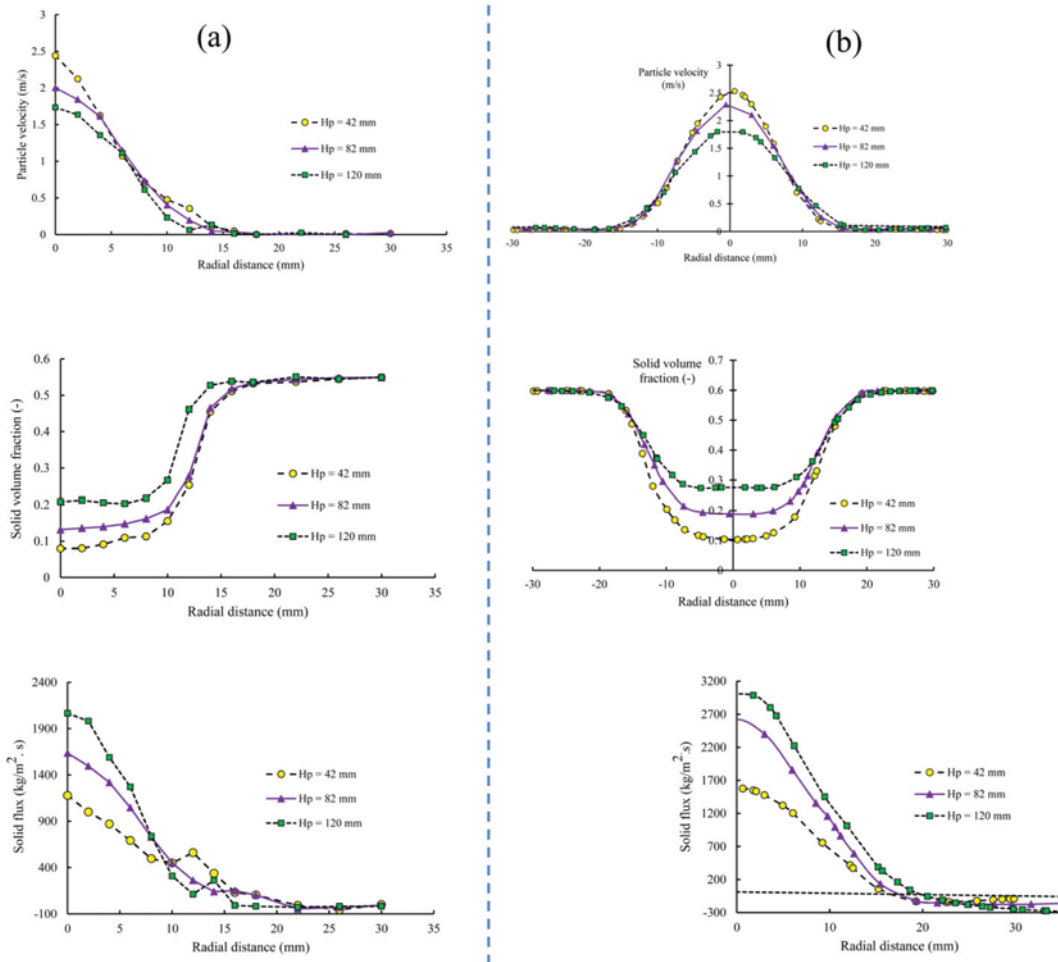
Fig. 4. Time-averaged particles velocity, solid volume fraction and solid flux for the spouted bed with the cone angle of 45°, U=57 m/s (1.25U$_{ms}$) and H$_b$=140 mm at different levels: (a) Experimental data, (b) Computational results.

are presented in Fig. 4 and compared with the corresponding experimental data of Kulah et al. [10]. The trends of CFD results for the particle velocity and solid volume fraction obtained for the bed with cone angle of 45° are quite similar to those obtained in the spouted bed with 30° cone angle. The computational results show that the solid velocity and solid concentration is symmetrical with respect to the bed axis. In the case of the conical spouted bed with 45° cone angle, the predicted particle velocities are in a good agreement with the experimental data; however, the solid volume fractions are slight over-predicted. Also, with an increase in the axial distance along the spout, the solid volume fraction increases, which is consistent with the earlier reports [38].

In addition to the particle velocity and solid volume fraction, the variations of solid flux calculated as $\alpha_s \rho_s V_s$ are studied and the results are shown in Fig. 4. Note that in calculation of solid flux, α_s and V_s are, respectively, the time averaged values of solids volume fraction and particle velocity. The experimental data and the CFD results show the same trend of variations. The computational model, however, over-predicts the solid flux perhaps due to the over-prediction of solid volume fraction. Nonetheless, the present CFD model predicts solid fluxes that are comparable with the experimental data of Lüle et al. [29] and in fact improves their 2D CFD results. Inter-
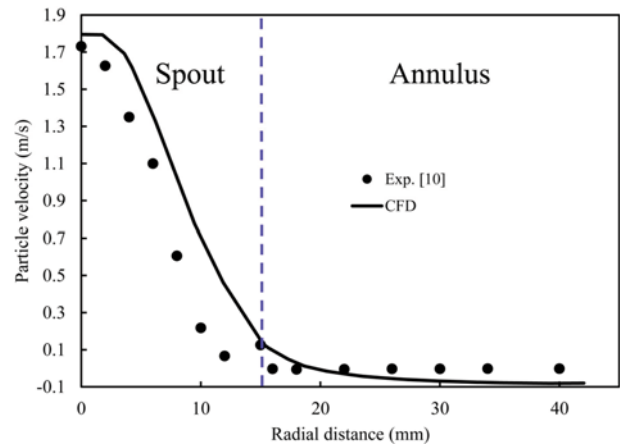

Fig. 5. Computed and measured time-averaged particle velocity in spout and annulus of the bed with a cone angle of 45°, U= 57 m/s and H$_b$=140 mm at H$_p$=120 mm.

estingly, the axial solid flux near the wall, which is downward, does not vary appreciably.

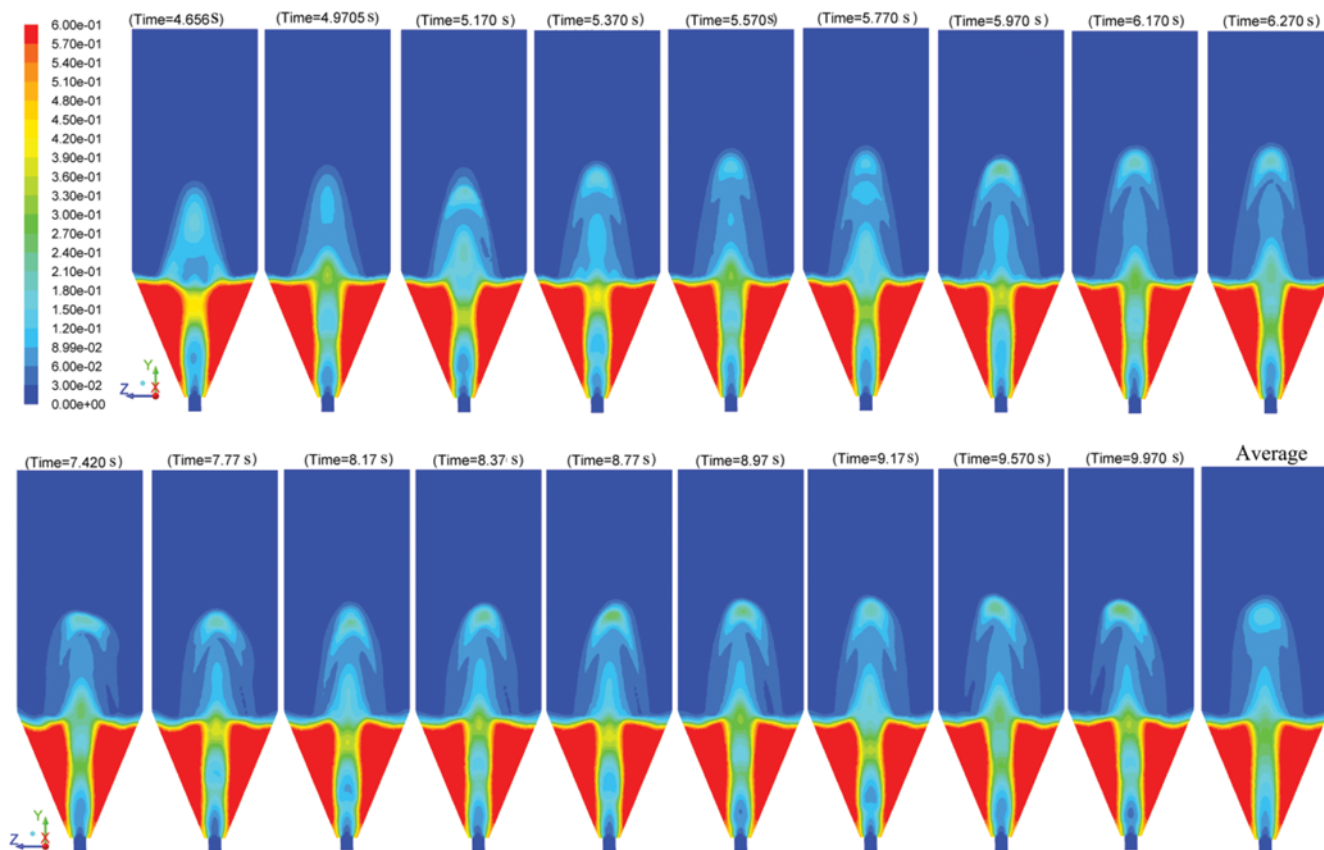Fig. 5 shows the particle velocity in spout and annulus, separately,

Fig. 6. Contour plots of time-averaged and instant solid volume fraction in the spouted bed with 45° cone angle, U=57 m/s and H_b=140 mm.

for the bed with cone angle of 45°, U=57 m/s and H_b=140 mm at a height of H_p=120 mm. The simulation results for particle velocity slightly over-predict the experimental data of [10] in the spout region. In the annulus region the simulation predicts a slight downward velocity, which is larger than that observed in the experiment, which is perhaps due to low friction between the particles in the computational model. Under-prediction of particle velocity in annulus region was previously reported for the Eulerian-Eulerian simulation of conical-cylindrical spouted beds, including light particles [39]. These discrepancies may be resolved by developing a more accurate frictional model for the Eulerian-Eulerian approach. This, however, is left for a future study.

Thein instantaneous and time-averaged contour plots of solid volume fraction in the spouted bed with 45° cone angle, U=57 m/s and H_b=140 mm are shown in Fig. 6. This figure shows distinct regions of spout, annulus and fountain for different times. Comparing this figure with Fig. 3, the fountain height and the concentration of particles in that region and its periphery do not change in time for the case of the spouted bed with 45° cone angle. In addition, particle concentration in the upper part of spout is lower compared to the bed with 30° cone angle. Nevertheless, connected bubbles appear along the spout at certain times. Finally, this figure shows that roughly stable spouting is established for the spouted bed with 45° cone angle.

Fig. 7 shows the axial particle velocities along the bed axis for the spouted bed with 45° cone angle and H_b=100 mm and 140 mm.
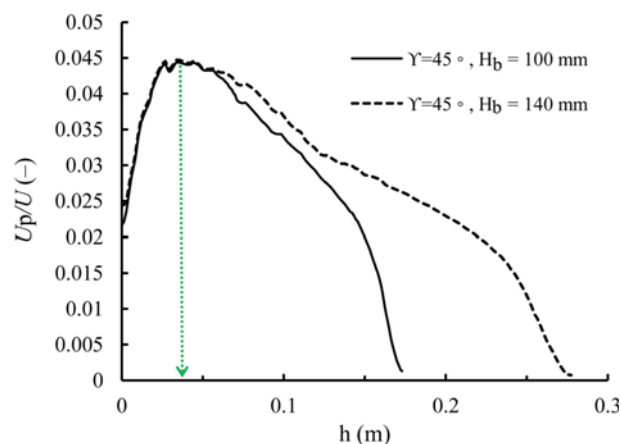

Fig. 7. Influence of static bed height on the axial particle velocities along the bed axis for the spouted bed with 45° cone angle at the same excess velocity over U_{ms}.

Here the inlet gas velocity U=1.25U_{ms}, where U_{ms} is the minimum spouting velocity corresponding to each static bed height as listed in Table 3. That is, the same excess velocity over the minimum spouting velocity is maintained for different bed height. The minimum spouting velocity is greatly affected by the static bed height [40-42]. Therefore, higher particle velocity in spout zone is expected for the case of H_b=140 mm. Thus, to have a meaningful compari-

son between particle velocities through the spout region for various static bed heights, the normalized time-averaged particle velocity, U_p/U, is shown in Fig. 7. The CFD results for the two static bed heights show that the particles in conical spouted bed of heavy particles quickly reach to their maximum velocity at short distances near the inlet. After their peak point, the flow gradually decelerates, and their velocity drops to zero in the fountain region. These trends of variation are consistent with the earlier studies of conical spouted beds of light particles [43]. Note that the maxi-

mum solid velocity occurs at the same level for both static bed heights, while the slope of decelerating particle velocity increases with a decrease in the static bed height.

Fig. 8 shows the influence of static bed height on the solid volume fraction along the bed axis for the spouted bed with 45° cone angle and H_b=100 mm and 140 mm and U=1.25U_{ms}. That is, the same excess inlet velocity over the minimum spouting velocity corresponding to each static bed height (Table 3) is used. The first solid volume fraction peaks shown by arrows in this figure are related to the high particle concentration regions in the upper part of spout, which are clearly seen in the average contour plots in Figs. 3 and 6. The second solid volume fraction peaks, near the top of the fountain, in Fig. 8, indicates the non-constant fountain due to establishing the incoherent spouting for the conical spouted beds operating with heavy particles. This trend of solid volume fraction along the spouted bed axis has been observed for spouted bed with light particles [44,45].

Fig. 9 shows instantaneous solid volume fraction contours in a conical-cylindrical spouted bed with 45° cone angle, when the solid particles fill the cone and part of the cylindrical region of the bed. Here U=57 m/s and H_b=200 mm. Distinct regions of spout, annulus and fountain can be seen from this figure. Fig. 9 also shows that in this case at certain times (t=8.85 s and t=14 s) choking of the spout zone occurs that leads to the vanishing the fountain region. The choking in spouted beds has adverse effects on gas-solid mixing, and heat and mass transfer. Thus, due to the potential for choking, the use of conical-cylindrical spouted beds for operating
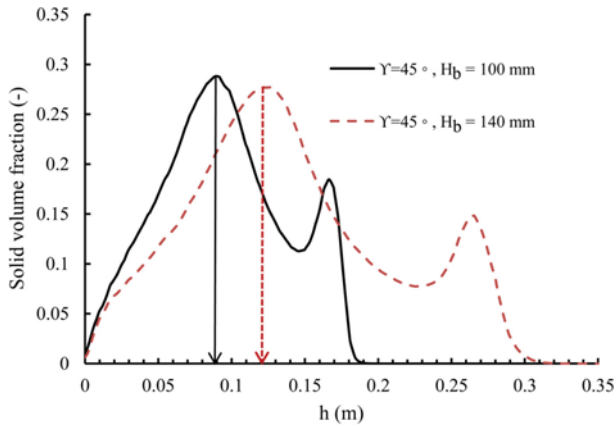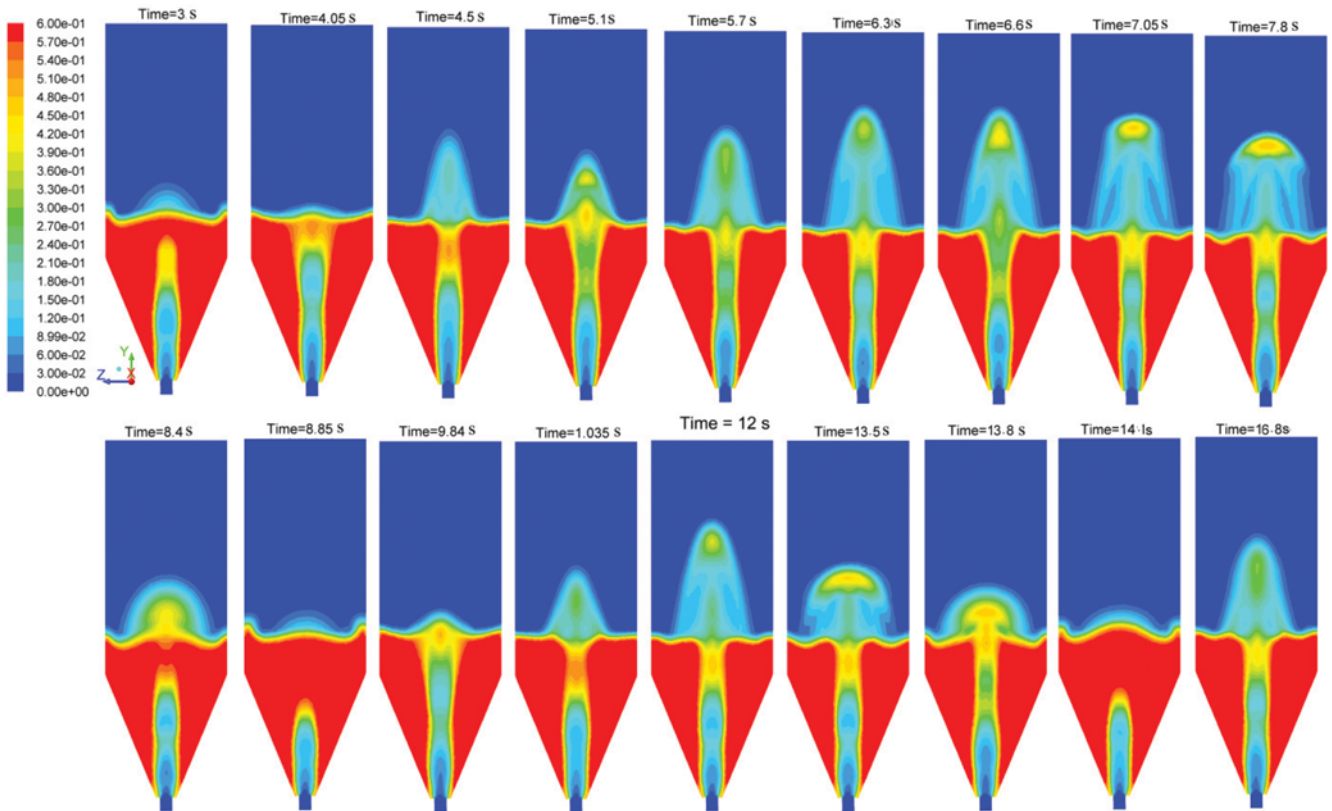

Fig. 8. Influence of static bed height on the solid volume fraction along the bed axis for the spouted bed with 45° cone angle at the same excess velocity over U_{ms}.

Fig. 9. Contour plots of instant solid volume fraction in the spouted bed with 45° cone angle, U=57 m/s and H_b=200 mm.
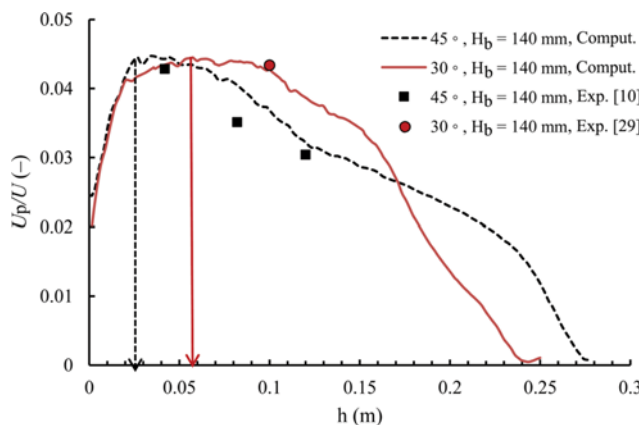
Fig. 10. Influence of bed cone angle on the particles velocity along the bed axis for the same static bed height and the same excess velocity over U_{ms}.

of heavy particles is not recommended. The simulation results shown in Fig. 9 also show that the solid volume fraction at the top as well as in the fountain core region is higher than that at the other part of the fountain, which agrees with the earlier reports [18,46,47].

Hydrodynamics of the conical spouted beds with cone angles of 30° and 45° is compared in Figs. 10, 11 and 12. Table 3 shows that the minimum spouting velocity and the corresponding inlet gas velocity $U=1.25U_{ms}$ for the bed with 45° cone angle are higher than those of the bed with 30° cone angle for the same static bed height; therefore, the normalized time-averaged particle velocity is compared here. Fig. 10 shows the axial particle velocities along the bed axis for the spouted beds with different cone angles and the same static bed height of $H_b=140$ mm. Here the inlet velocity of $U=1.25U_{ms}$ is used so that the relative excess velocity over the minimum spouting velocity is the same. Good agreements between the CFD simulation results and the available measured data for both conical spouted beds with cone angles of 30° and 45° are found.

The CFD results reveal that both bed configurations have the same maximum particle velocity in the spout region, but the locations of peak velocities as shown by arrows in the Fig. 10 are different. In addition, the bed with cone angle of 30° shows a flatter profile for the particle velocity in the spout region compared to that of the bed with 45° cone angle.

Fig. 11 shows the solid volume fraction distribution along the bed axis for the spouted beds with different cone angles and the same static bed height of $H_b=140$ mm and inlet gas velocities of $1.25U_{ms}$. The solid volume fraction increases along the bed axis and reaches its maximum value in the upper region of spout, and then decreases in fountain region. This trend is seen for both beds with cone angles of 30° and 45. Also, the computational results for the solid volume fraction for the bed with cone angle of 45° are in general agreement with the limited experimental data for the same cone angle. Fig. 11 also shows that the predicted maximum value of solid volume fraction for the bed with cone angle of 30° is higher than that of the bed with 45° cone, and appears at a slightly higher distance from the inlet. It is noteworthy that due to extremely incoherent behavior of the particles in the fountain zone for the bed with cone angle of 30° in comparison with the 45° cone angle, the time averaged fountain height for the former is lower than that of the latter, while the maximum solid concentration for the 45° cone angle bed is higher than that of the 30° cone angle. These trends are clearly observed in Figs. 10 and 11.

Fig. 12 shows the variation of the predicted spout diameters for the conical spouted beds for different static bed heights and different cone angles. This is determined by tracing the particle velocity over the entire spout and annulus regions and detecting the point where particle velocities pass through zero. The CFD model predicts that at the same static bed height ($H_b=140$ mm), with an increase in the cone angle of the bed, the spout diameter also increases.
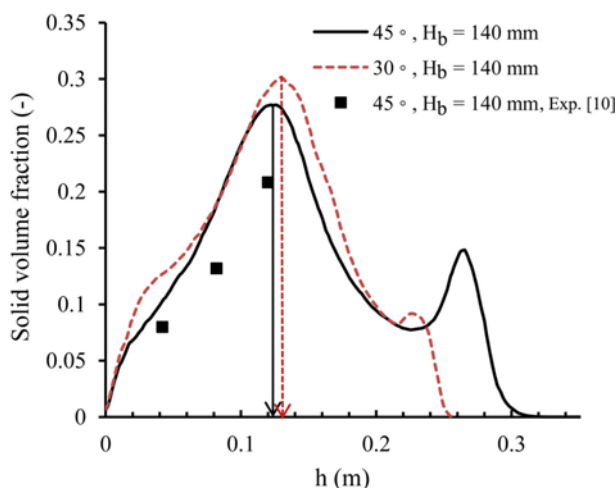

Fig. 11. Influence of bed cone angle on the solid volume fraction along the bed axis for the same static bed height and the same excess velocity over U_{ms}.
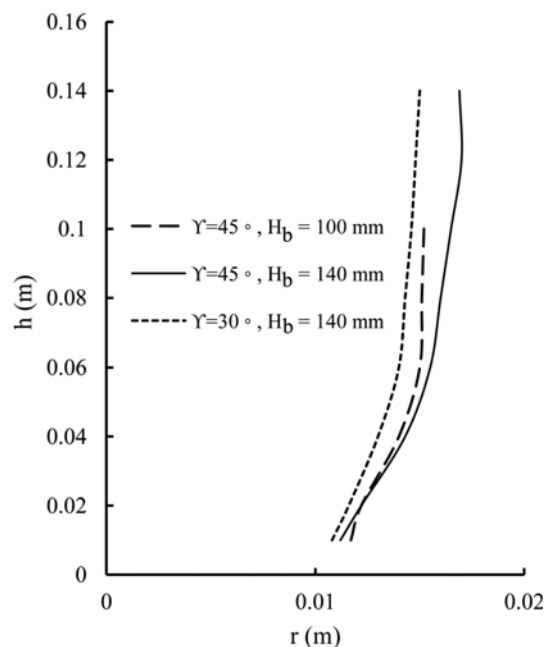

Fig. 12. Computed spout diameter for the conical spouted beds with different static bed height and cone angle.

In addition, for spouted beds with the same cone angle (45°), the spout diameter increases with increasing the static bed height. Fig. 12 also shows that the spout diameter increases roughly monotonically with height for beds with heavy particles. This observation agrees with experimental observation [48], and is unlike the conical spouted beds of light particles [25].

Another issue addressed in the present study is the simulations of spouted beds using half-column instead of full-column. Previously, He [45] measured and compared some hydrodynamics parameters for full and half columns. It this study, to examine the influence of bed geometry on the particle velocity, both full-column and half-column are simulated under the same condition. Attention was given to the question that whether the flat plate side of the half-column

model affects the particle velocity in the spout region.

The CFD results for the time-averaged particles velocity for H_p= 100 mm for the full and half columns with 30° cone angle, U=38.6 m/s and H_b=140 mm are plotted in Fig. 13 and compared with the experimental data of [29] for the full column. The predicted particle velocity profile for the full column is in good agreement with the experimental data. The simulated particle velocity for the half column is similar to the full column in most of the section except near the flat plate side of the half column, where the local particle velocities in the half-column are markedly lower than those in the full-column. Note the particle velocity near the side plate is lower than the peak value a few millimeters away from the side plate,
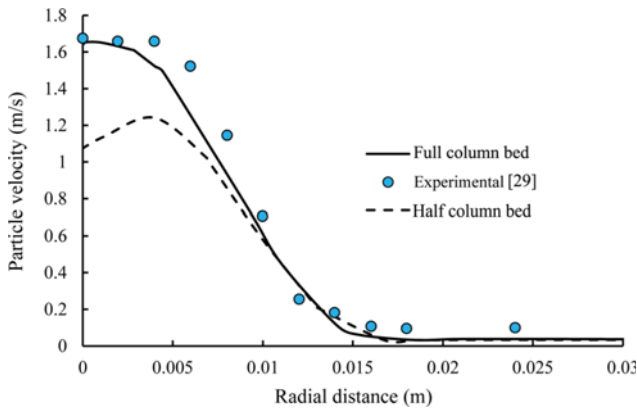

Fig. 13. Time-averaged particles velocity for the full and half columns with 30° cone angle, U=38.6 m/s and H_b=140 mm at H_p=100 mm.
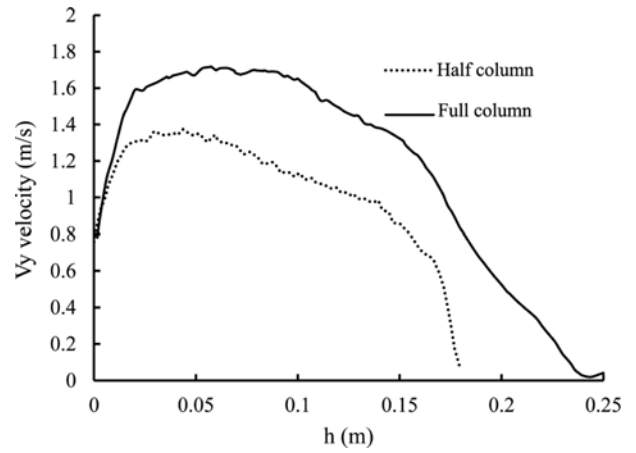

Fig. 14. Axial particle velocities along the bed axis for full and half columns at the identical conditions of H_b=140 mm and U=38.6 m/s.
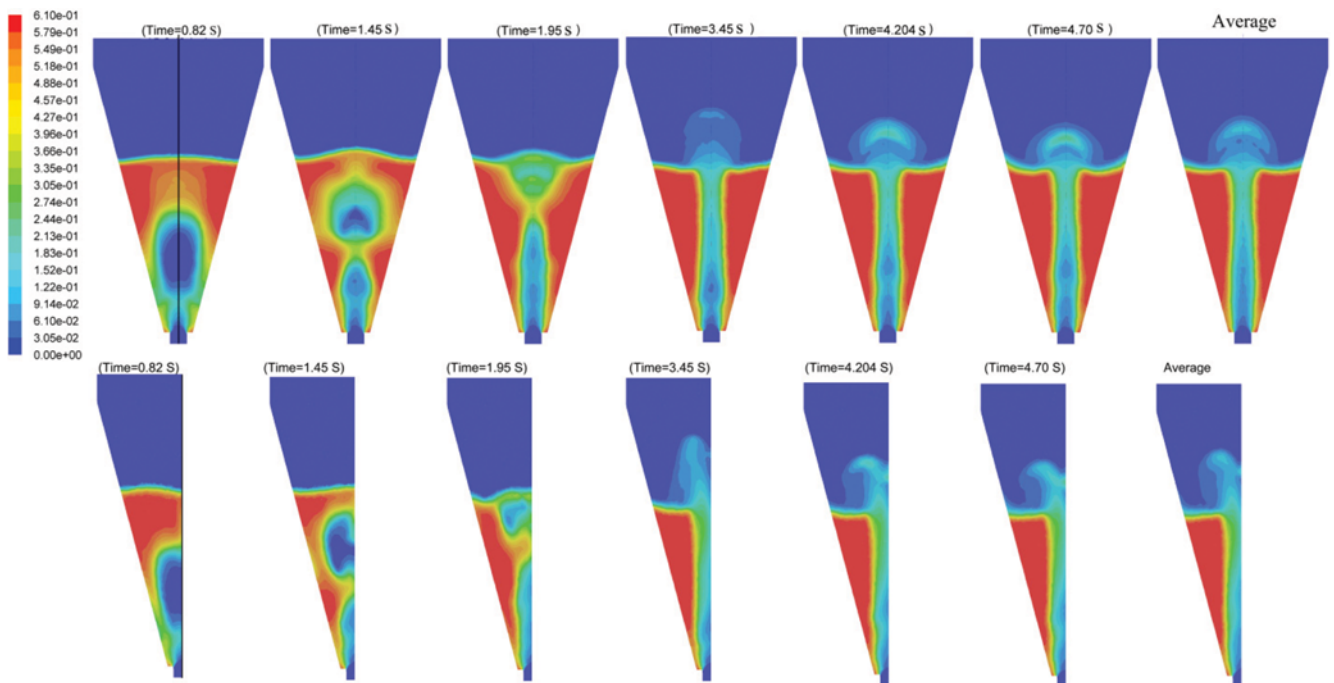

Fig. 15. Contour plots of solid volume fraction for the semi-conical spouted bed (half-column) with 30° cone angle, U=38.6 m/s, and H_b= 140 mm as instantaneous and time-averaged.
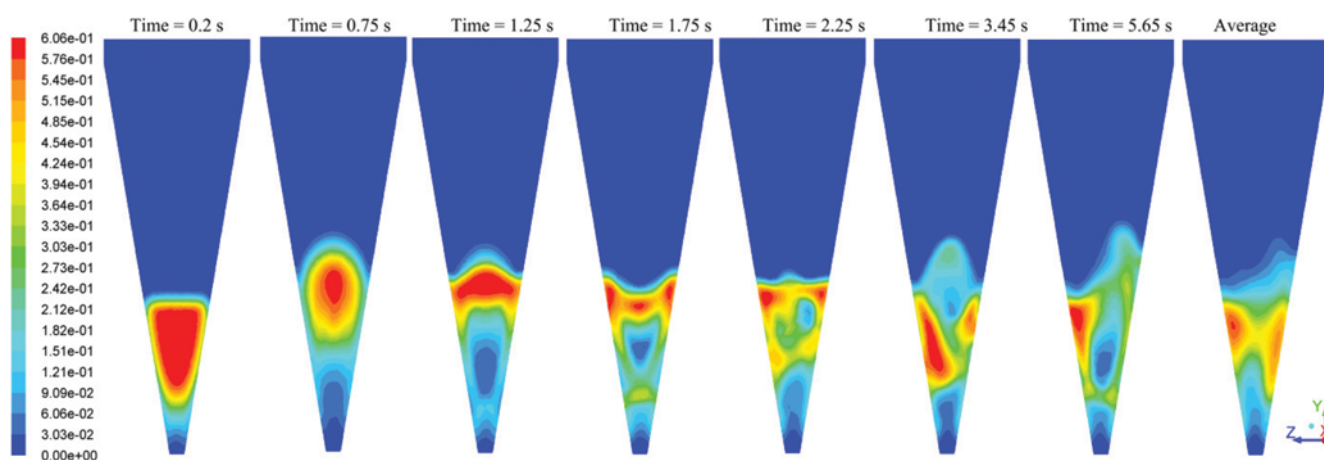
Fig. 16. Influence of cone bottom diameter on the CFD results of the spouted bed with 30° cone angle, U=38.6 m/s, and H_b=140 mm.

which is in agreement with the earlier findings [45]. This is, due to the effect of no-slip condition on the gas flow and the wall-friction on the particle flow.

Fig. 14 shows the axial particle velocities along the bed axis for full and half columns under the identical conditions of H_b=140 mm and U=38.6 m/s ($1.25U_{ms}$) for the heavy particles. Note that for the half column, the axis is on the surface of the side plate. Therefore, for particle velocity along the axis of the half-column, the points closest to the plate are used. While the trends of particle velocity profiles along the spout axis are similar, the magnitude of the particle velocities in the half-column is much lower than the corresponding velocities in the full-column.

Using the fiber probe technique, He [45] experimentally studied the effect of the side flat plate of the half-column on the particle velocity in the spout region of a conical-cylindrical spouted bed with light particles. The trend of variation the present CFD study shown in Fig. 14 is almost identical to that of the experimental data of [45]. From the above discussion, it may be concluded that the half-column cannot accurately describe the hydrodynamics of a full-column with respect to the particle velocity in the spout for the conical spouted beds operating with heavy particles.

Fig. 15 depicts the contour plots of solid volume fraction at various times and time-averaged solid volume fraction for the semi-conical spouted bed (half-column) with 30° cone angle, with U= 38.6 m/s, and H_b=140 mm. Note that the contours on the top row are for the solid volume fraction on the surface of side plate and the bottom row contours are for the plane that is perpendicular to the side plates. The intersection of these two planes, which is identified by a black line, is shown in the first contour on the left side. The process of spout formation is clearly seen from this figure. This figure shows that the gas phase injected from the nozzle expands along the spout axis and creates a bubble that is separated from subsequent connected bubbles at the nozzle. Finally, roughly stable spout is established. It is seen that the flow behavior in the spout of the half column is different than that observed for the full-column in Fig. 3.

The time-averaged bed pressure drop is also investigated for half and full columns. The computed time-averaged pressure drop for the half and full columns with the identical conditions of H_b=

140 mm and U=38.6 m/s ($1.25U_{ms}$) are, respectively, 3,725 Pa and 3,785 Pa, which agree well with the measured value of 3,764 Pa. It appears that the time-averaged bed pressure drops of the half-column and full-column are pretty much the same, which is consistent with the finding of previous studies [45,49].

The influence of cone bottom diameter on the CFD results for the case of the spouted bed with cone angle was also investigated. For this purpose, the cone bottom diameter, D_i, was assumed to be equal to the nozzle diameter, D_0. That is, the bottom space around the nozzle was omitted. Fig. 16 shows the contour plots of solid volume fraction at various times and time-averaged solid volume fraction for the spouted bed with 30° cone angle, for U=38.6 m/s, H_b=140 mm and $D_i=D_0$. It is observed that the distinct regions of spout, fountain and annulus are not formed under this configuration. In addition, due to the low cone angle the bed hydrodynamics becomes similar to that of a tapered fluidized bed. That is, the particle flow pattern in this case is quite similar to corresponding flow pattern observed in tapered fluidized beds [50,51].

CONCLUSIONS

The gas/solid flow behavior of the conical-cylindrical spouted beds operating with heavy particles, zirconia, with density of ρ= 6,050 kg/m³ was studied using the FLUENT CFD code. The Eulerian-Eulerian TFM incorporating the KTGF was used and the full 3D geometry of the bed was analyzed. The effects of key design parameters, cone angle, static bed height, and cone bottom diameter, were evaluated. Simulation results for the full conical spouted bed were compared with those for the half bed. Based on the presented CFD results, the following conclusions were drawn:

1) The CFD model predicts the axial particle velocity along the spout and in the radial direction with reasonable accuracy, while slightly over-predicts the solid volume fraction in the spout.

2) The solid flux in the spout increases with an increase in the distance from nozzle.

3) The computational model under-predicts the particles velocity in the annulus region. It is conjectured that using a more suitable constitutive equation for the frictional stress between the particles could improve the model predictions in this region.

4) The cone angle greatly affects the fountain height and resulting in the incoherent spouting for smaller cone angles.

5) Conical spouted bed with different static bed heights studied showed roughly the same maximum normalized velocity (U_p/U) occurring at roughly the same location on the spout axis for the same excess velocity over the minimum spouting, while the corresponding maximum solid concentrations occur at different locations.

6) For a gas inlet velocity with same excess magnitude over the minimum spouting velocity, the conical spouted beds with different cone angles showed identical maximum normalized velocity (U_p/U) occurring at different position on the spout axis. The corresponding peak solid concentrations, however, occurred at approximately the same position, but with different magnitude.

7) The conical-cylindrical spouted beds operating with heavy particles showed the periodic occurrence of choking in the spout region.

8) For the cases studied, at the same static bed height and the same excess inlet gas velocity over the minimum spouting speed, the spout diameter increased with an increase in the bed cone angle. Also, under identical conditions, the spout diameter increased when the static bed height increased. In addition, for the conical spouted beds operating with heavy particles, the spout diameter increased monotonically with height.

9) The half-column model with a wall at the mid-plane does not properly represent the particle velocity in the spout region of a full-column conical spouted bed operating with heavy particles.

10) Changes in the cone bottom diameter significantly affected the particle flow pattern in the spouted bed for both cone angles studied.

NOMENCLATURE

C_D : drag coefficient [-]
d_s : particle diameter [m]
D_0 : diameter of the spout gas inlet [m]
D_i : cone bottom diameter [m]
D_c : diameter of the bed [m]
H_b : static bed depth [mm]
H_p : axial distance of the optical probe from the bed bottom [mm]
e_s : particle-particle restitution coefficient [-]
e_w : particle-wall restitution coefficient [-]
g : acceleration due to gravity [m/s^2]
g_0 : radial distribution coefficient [-]
$\bar{I}$: stress tensor [-]
I_{2D} : second invariant of the deviatoric stress tensor [-]
$k_{\Theta s}$: diffusion coefficient for granular energy [kg/m s]
β : gas-solid momentum exchange coefficient [kg/m^3 s]
β_{Ergun} : gas-solid momentum exchange coefficient by Ergun equation [kg/m^3 s]
β_{Wen-Yu} : gas-solid momentum exchange coefficient calculated by Wen-Yu equation [kg/m^3 s]
P : pressure [N/m^2]
P_s : solids pressure [N/m^2]
t : time [s]
U : superficial gas velocity [m/s]

U_{ms} : minimum spouting velocity [m/s]
v_i : velocity [m/s]

Greek Letters

α_i : volume fraction [-]
γ : angle of the conical section [degree]
γ_s : the collisional dissipation of energy [kg/s^3 m]
Θ_s : granular temperature [m^2/s^2]
λ_s : solid bulk viscosity [kg/m s]
μ_i : shear viscosity [kg/m s]
ρ_i : density [kg/m^3]
$\bar{\tau}_i$: stress tensor [N/m^2]
ϕ : angle of internal friction [degree]
φ : specularity coefficient [-]

Subscripts

col : collision
fr : friction
kin : kinetic
g : gas
p : particle
q : phase type (solid or gas)
s : solids
T : stress tensor

REFERENCES

1. P. E. Gishler, *Can. J. Chem. Eng.*, **61**, 267 (1983).
2. A. Kmiec and R. G. Szafran, *Kinetics of Drying of Microspherical Particles in a Spouted Bed Dryer with a Draft Tube*, In Proceedings of the 12th International Drying Symposium (IDS 2000), Elsevier Science B.V.: Amsterdam (2000).
3. D. J. E. Harvie, T. A. G. Langrish and D. F. A. Fletcher, *Trans. Inst. Chem. Eng.*, **80**, 163 (2002).
4. H. Ichikawa, M. Arimoto and Y. Fukumori, *Powder Technol.*, **130**, 189 (2003).
5. S. I. Al-Mayman and S. M. Al-Zahrani, *Fuel Process Technol.*, **80**, 169 (2003).
6. M. Khoshnoodi and F. J. Weinberg, *Combust. Flame*, **33**, 11 (1978).
7. S. R. A. Kersten, W. Prins, B. van der Drift and W. P. M. van Swaaij, *Chem. Eng. Sci.*, **58**, 725 (2003).
8. C. Luo, K. Aoki, S. Uemiya and T. Kojima, *Fuel Process Technol.*, **55**, 193 (1998).
9. G. Lopez, J. Alvarez, M. Amutio, A. Arregi, J. Bilbao and M. Olazar, *Energy*, **107**, 493 (2016).
10. G. Kulah, S. Sari and M. Koksal, *Ind. Eng. Chem. Res.*, **55**, 3131 (2016).
11. X. Liu, W. Zhong, X. Jiang and B. Jin, *AIChE J.*, **61**, 58 (2015).
12. L. Qian, Y. Lu, W. Zhong, X. Chen, B. Ren and B. Jin, *Can. J. Chem. Eng.*, **91**, 1793 (2013).
13. V. S. Sutkar, N. G. Deen, A. V. Patil, F. E. A. J. Peters, V. Salikov, S. Heinrich, S. Antonyuk and J. A. M. Kuipers, *AIChE J.*, **61**, 1146 (2015).
14. X. Chen, B. Ren, Y. Chen, W. Zhong, D. Chen, Y. Lu and B. Jin, *Can. J. Chem. Eng.*, **91**, 1762 (2013).
15. J. F. Saldarriaga, R. Aguado, H. Altzibar, A. Atxutegi, J. Bilbao and

M. Olazar, *J. Taiwan Inst. Chem. Eng.*, **60**, 509 (2016).

16. S. Azizi, S. H. Hosseini, M. Moraveji and G. Ahmadi, *Particuology*, **8**, 415 (2010).

17. M. Fattahi, S. H. Hosseini and G. Ahmadi, *Appl. Therm. Eng.*, **105**, 385 (2016).

18. S. H. Hosseini, G. Ahmadi and M. Olazar, *Powder Technol.*, **246**, 303 (2013).

19. S. H. Hosseini, G. Ahmadi and M. Olazar, *J. Taiwan Inst. Chem. Eng.*, **45**, 2140 (2014).

20. S. H. Hosseini, M. Fattahi and G. Ahmadi, *J. Taiwan Inst. Chem. Eng.*, **58**, 107 (2016).

21. S. H. Hosseini, *Prog. Comput. Fluid Dyn.*, **16**, 78 (2016).

22. S. H. Hosseini, G. Ahmadi, B. S. Razavi and W. Zhong, *Energy Fuels*, **24**, 6086 (2010).

23. S. H. Hosseini, M. Fattahi and G. Ahmadi, *Powder Technol.*, **279**, 301 (2015).

24. S. Moradi, A. Yeganeh and M. Salimi, *Appl. Math. Model*, **37**, 1851 (2013).

25. M. J. San Jose, M. Olazar, S. Alvarez, A. Morales and J. Bilbao, *Ind. Eng. Chem. Res.*, **44**, 193 (2005).

26. M. J. San Jose, S. Alvarez, A. Morales, M. Olazar and J. Bilbao, *Chem. Eng. Res. Des.*, **84**, 487 (2006).

27. J. Zhou and D. D. Bruns, *Can. J. Chem. Eng.*, **90**, 558 (2012).

28. S. Pannala, C. S. Daw, C. E. A. Finney, D. Boyalakuntla, M. Syamlal and T. J. O'Brien, *Chem. Vapor Depos.*, **13**, 481 (2007).

29. S. Ş. Lüle, U. Colak, M. Koksal and G. Kulah, *Chem. Vap. Depos.*, **21**, 1 (2015).

30. N. Setarehshenas, S. H. Hosseini, M. Nasr Esfahany and G. Ahmadi, *J. Taiwan Inst. Chem. Eng.*, **64**, 146 (2016).

31. D. G. Schaeffer, *J. Differ. Equat.*, **66**, 19 (1987).

32. C. K. K. Lun, S. B. Savage, D. J. Jeffrey and N. Chepurniy, *J. Fluid Mech.*, **140**, 223 (1984).

33. L. Huilin, D. Gidaspow, J. Bouillard and L. Wentie, *Chem. Eng. J.*, **95**, 1 (2003).

34. P. C. Johnson and R. Jackson, *J. Fluid Mech.*, **176**, 67 (1987).

35. S. H. Hosseini, R. Rahimi, M. Zivdar and A. Samimi, *Korean J. Chem. Eng.*, **26**, 1405 (2009).

36. R. Bettega, C. A. da Rosa, R. G. Corrêa and J. T. Freire, *Ind. Eng. Chem. Res.*, **48**, 11181 (2009).

37. Y. Behjat, S. Shahhosseini and M. Ahmadi Marvast, *Int. Commun. Heat Mass*, **37**, 935 (2010).

38. M. J. San Jose, M. Olazar, S. Alvarez and J. Bilbao, *Ind. Eng. Chem. Res.*, **37**, 2553 (1998).

39. W. Du, X. Bao, J. Xu and W. Wei, *Chem. Eng. Sci.*, **61**, 1401 (2006).

40. S. H. Hosseini, M. Karami, M. Olazar, R. Safabakhsh and M. Rahmati, *Ind. Eng. Chem. Res.*, **53**, 12639 (2014).

41. K. B. Mathur and P. E. Gishler, *AIChE J.*, **1**, 157 (1955).

42. M. Olazar, M. J. San José, A. T. Aguayo, J. M. Arandes and J. Bilbao, *Chem. Eng. J. Biochem. Eng.*, **55**, 27 (1994).

43. M. Olazar, M. J. San Jose, S. A. Morales and J. Bilbao, *Ind. Eng. Chem. Res.*, **37**, 4520 (1998).

44. W. Sobieski, *Dry Technol.*, **26**, 1438 (2008).

45. R. Béttega, R. G. Corrêa and J. T. Freire, *Study of the Scale-Up Relations for Spouted Beds using CFD*, 19th Int. Cong. Mech. Eng., Brasília DF 5-9 (2007).

46. Y. L. He, *Hydrodynamic and Scale-up Studies of Spouted Beds*, University of British Columbia, Ph.D. Thesis (1995).

47. L. Huilin, H. Yurong, L. Wentie, D. Jianmin, D. Gidaspow and J. Bouillard, *Chem. Eng. Sci.*, **59**, 865 (2004).

48. S. Sari, A. Polat, D. Zaglanmis, G. Kulah and M. Koksal, *Hydrodynamics of Conical Spouted Beds with High Density Particles*, Proceedings of 10th International Conference on Circulating Fluidized Beds and Fluidization Technology, Sun River, Idaho, U.S.A. (2011).

49. S. Sari, G. Kulah and M. Koksal, *Exp. Therm. Fluid Sci.*, **40**, 132 (2012).

50. D. C. Sau and K. C. Biswal, *Appl. Math. Model*, **35**, 2265 (2011).

51. S. Liyan, X. Weiguo, L. Guodong, S. Dan, L. Huilin, T. Yanjia and L. Dan, *Chem. Eng. Sci.*, **84**, 170 (2012).